Detection of Damage in Operating Wind Turbines by Signature Distances

Dylan D. Chase[1], Kourosh Danai[2], Mathew A. Lackner[3], and James F. Manwell[4]

[1,2,3,4] *Dept. of Mechanical and Industrial Engineering, Univ. of Massachusetts Amherst, Amherst, Massachusetts, 01003, USA*
ddchase@student.umass.edu
danai@ecs.umass.edu
manwell@ecs.umass.edu
lackner@ecs.umass.edu

ABSTRACT

Wind turbines operate in the atmospheric boundary layer and are subject to complex random loading. This precludes using a deterministic response of healthy turbines as the baseline for identifying the effect of damage on the measured response of operating turbines. In the absence of such a deterministic response, the stochastic dynamic response of the tower to a shutdown maneuver is found to be affected distinctively by damage in contrast to wind. Such a dynamic response, however, cannot be established for the blades. As an alternative, the estimate of blade damage is sought through its effect on the third or fourth modal frequency, each found to be mostly unaffected by wind. To discern the effect of damage from the wind effect on these responses, a unified method of damage detection is introduced that accommodates different responses. In this method, the dynamic responses are transformed to surfaces via continuous wavelet transforms to accentuate the effect of wind or damage on the dynamic response. Regions of significant deviations between these surfaces are then isolated in their corresponding planes to capture the change signatures. The image distances between these change signatures are shown to produce consistent estimates of damage for both the tower and the blades in presence of varying wind field profiles.

1. INTRODUCTION

Condition monitoring of wind turbines has become increasingly more important as progressively larger turbines are situated in remote locations that are exorbitantly costly and time-consuming to inspect. This exorbitant cost of access and routine inspection also precludes the use of nondestructive methods based on ultrasound or acoustics, which require overhaul

and disassembly of the turbines and their blades. Therefore, the most promising recourse is the development of an automated structural health monitoring (SHM) system that relies on remote sensory data to continually assess the condition of the turbine tower and its blades.

Among the variables influenced by damage, structural vibration is particularly easy to measure by remote sensing as the basis of an automated SHM system. Vibration-based damage detection can be inverse or direct (Farrar & Doebling, 1997; Carden & Fanning, 2004; Santos, Maia, Soares, & Soares, 2008). Inverse methods update the structural model periodically to duplicate the measured response. They then estimate the physical properties of the structure from the updated model to asses the health of the structure (e.g., reduction of stiffness due to the onset of a crack or loosening of a connection) (Friswell, 2007). Inverse models, therefore, require not only an accurate model of the structure but also a complete knowledge of the input conditions that produce the measured vibration. This, unfortunately is never true for in-operation wind turbines because of unknowable wind conditions at various locations of the blade (i.e., wind profile). In contrast to inverse methods, direct methods of damage detection focus directly on identifying the effect of damage on the dynamic response of the structure (Danai, Civjan, & Styckiewicz, 2011) or its modal properties (Doebling, Farrar, Prime, & Shevitz, 1996). Given that dynamic response histories are never the same for operating wind turbines due to variable wind conditions, a challenge in health monitoring of wind turbines is to identify the dynamic time history or modal properties that are distinctly affected by damage as opposed to wind.

We have identified a shutdown maneuver of the turbine, consisting of pitching the blades to feather and braking, to produce a dynamic response that is distinctly affected by tower damage. However, a dynamic response representative of blade damage could not be identified. The blade response during the shutdown maneuver is considerably more sensi-

tive to the wind profile because of the continuous pitching of the blades during the maneuver and the cyclic and stochastic loads on the blades that depend on the wind profile. This makes the blade time history response more sensitive to the wind profile and to the operating and initial conditions at the time of the maneuver. As a recourse, blade damage estimation is performed via modal analysis. Several studies have reported the effect of structural damage on the higher modal frequencies and the corresponding mode shapes (Farrar & Doebling, 1997). By following their lead, we have found in our studies that blade damage, as represented by localized reduction of stiffness coefficients, reduces the third and fourth natural frequencies of the blade independent of the wind conditions. Our studies also indicate that these frequency shifts (off-sets) are proportional to the level of damage and that their estimates are sensitive to the location of vibration measurement as well as the damage location.

Even though the damage effects are visually distinct from the wind effect, their isolation across different measurement locations and wind conditions is not robustly possible in either the time or frequency domain. The contribution of this paper, therefore, is to introduce a method of damage detection that differentiates the effect of damage from the wind on vibration time histories or their spectra, alike. The differentiation between the damage and wind effects in this method is facilitated by transforming the corresponding data series to surfaces in the time-scale or frequency-scale domain via continuous wavelet transforms (CWTs). The difference between the pairs of surfaces, comprising the dynamic response and its baseline, is characterized by isolating regions of the plane that represent localized significant deviations between them. The image distances between these isolated regions are then found to be significantly larger for damages than wind effects. They are, therefore, used as estimates of the damage for different measurement locations and wind conditions.

2. WIND TURBINE MODEL

Damage is characterized in this study by a reduction of tower or blade stiffness, which would occur from fatigue, cracking, loosening of connections or delamination. Both the tower and blade damage are estimated from the acceleration of the tower and blade. The wind turbine is modeled using the aero-elastic design code FAST (Jonkman & Buhl Jr, 2005) developed by the National Wind Technology Center (NWTC). The NWTC program Modes is used to calculate the blade and tower mode shapes (Buhl, n.d.) and TurbSim is used to simulate full-field, turbulent, stochastic wind files (Kelly & Jonkman, n.d.). For this study the NREL 5-MW reference wind turbine (Jonkman, Butterfield, Musial, & Scott, 2009) is simulated to replicate the effect of damage in large scale wind turbines.

In FAST distributed properties are specified at discrete locations along the length of the tower and the blades. The properties of the blade include: (1) flap-wise stiffness, (2) edge-

wise stiffness, (3) torsional stiffness, and (4) mass per unit length, and those of the tower are the fore-aft and side-side stiffness coefficients. The stiffness values are also inputs to the program Modes, which computes the mode shapes of the tower and the blades. The NREL 5-MW reference offshore wind turbine consists of a tower that is 87.6 m high, with its distributed properties specified at 11 nodes, and blades that are 63 m in length, with their distributed properties specified at 49 span-wise nodes. The location of the distributed properties are shown in Fig. 1. Tower damage is simulated at six locations by reduction of the corresponding parameters p1 through p6. Blade damage is simulated at three locations: (1) close to the root, (2) mid-span, and (3) tip of the blade. The geometry of the blade is much more complicated than that of the tower and therefore many more stiffness values need to be specified for each blade. Since the reduced stiffness value of an individual node has no discernable effect on the blade vibration, damage at a location is represented by the reduced stiffness of six nodes associated with that location. Furthermore, damage level is simulated by the proportional reduction of the corresponding stiffness values. For instance, 30% damage at the blade mid-span is simulated by a 30% reduction in the flap-wise stiffness values of its 6 mid-span nodes, denoted by parameter p2 in Fig. 1. The other parameters p1 and p3, associated with the other blade locations, are also shown in Fig. 1.

FAST balances forces at a set of locations along the length of the tower or the blade. For the NREL 5 MW wind turbine model, FAST balances the forces at 20 nodes along the length of the tower and 17 analysis nodes along the length of the blade. FAST can be configured to output data at any of these analysis nodes, but for a given simulation, data can only be output at 9 blade and 9 tower analysis nodes. Therefore, 9 analysis nodes were chosen on the tower and blade each, as also shown in Fig. 1. At each of the sensor locations, fore-aft acceleration is recorded for the tower and flap-wise acceleration for the blade.

The primary input to the wind turbine is the stochastic wind input profile. In order to consider the effect of different wind profiles, five different wind data sets (referred to as Wind 1 to Wind 5) were generated by TurbSim to represent wind speeds in a square grid of 31 by 31 elements. At each grid location, the wind speed and direction are represented by a vector. The x-direction wind speeds of the five wind profiles at the hub location are shown in Fig. 2. Each of the wind profiles uses the Risø smooth terrain spectral model, has an average wind speed of 12 m/s and a power law exponent of 0.143, to account for wind shear. The turbulence intensity of the five wind profiles are: 0.1063, 0.8617, 0.10088, 0.11187 and 0.11418. In addition to wind profiles, other inputs of interest include the dynamics associated with yawing the wind turbine and pitching the wind turbine blades. Pitching of the wind turbine blade occurs in normal operation when the wind
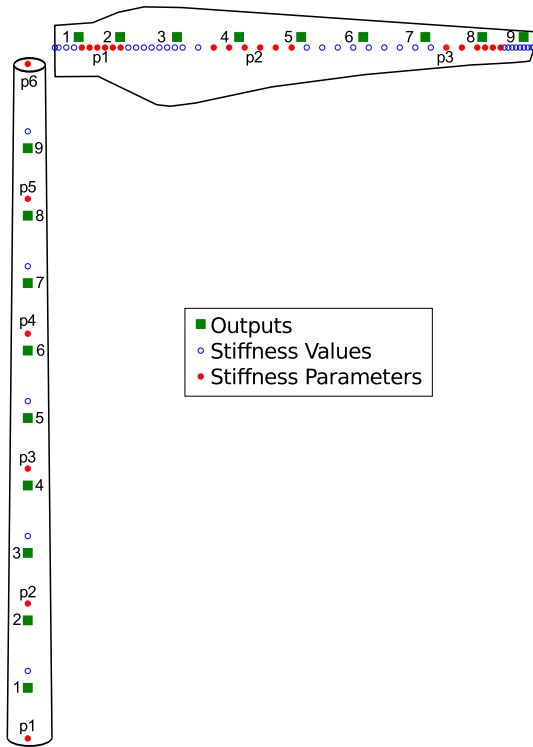
Figure 1: Schematics of the tower and a blade showing the locations of the distributed parameters, the parameters associate with each damage, and the measurement locations. The symbol, ○, corresponds to the locations where blade flap-wise stiffness values are defined. The symbol, •, corresponds to the flap-wise stiffness values associated with damage. The stiffness values of six node groups associated with the damage at that location are labeled as p1 - p3. The symbol, ■, corresponds to the nine locations where tower fore-aft or blade flap-wise acceleration is recorded.

speed is above the rated wind speed of the wind turbine and also during shutdown when the blade is pitched out of the wind.

3. DYNAMIC RESPONSE OVERVIEW

A requisite of direct damage detection is the presence of a deterministic dynamic response that would be representative of the damage. This deterministic response recorded for the healthy system is then used as the baseline for identifying the damage from the dynamic responses that are periodically acquired for evaluating the health of the system. Ordinarily, such a deterministic dynamic response would comprise the response to a uniform excitation of the system (e.g., harmonic excitation of the structure by an eccentric mass shaker) (Danai et al., 2011). However, such a deterministic dynamic response cannot be established for wind turbines, due to the stochastic and ever present effect of wind on the vibration of in-operation wind turbines. A first task of this
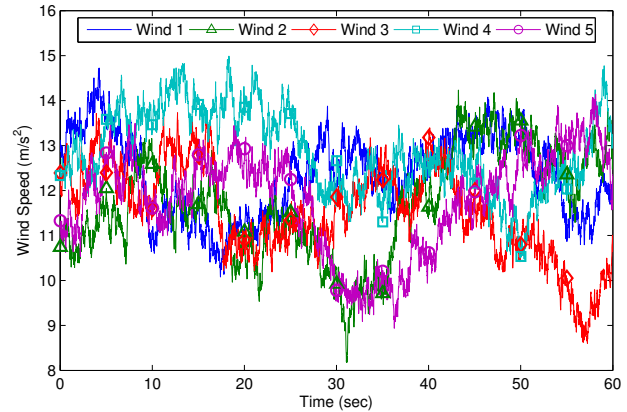
Figure 2: Hub height horizontal, perpendicular to the rotor, wind speeds of the five wind input profiles during a 60 sec time window

research, therefore, is identifying a dynamic response that despite its stochastic nature would distinctly represent the effect of damage in contrast to wind. To this end, we have explored the response of the turbine to a shutdown maneuver, consisting of pitching the blade to feather and applying the brake, to provide uniform initial conditions for the free response of the turbine. The acceleration of the tower and blade under different conditions (healthy and a faulty condition with two different wind profiles) before and after the application of this shutdown maneuver is shown in Fig. 3. For improved clarity, these acceleration time series are also shown in Fig. 4 for a smaller time window directly after the application of the shutdown maneuver in the 500-508 s time window. Vibration time series of the tower during the shutdown maneuver, shown in the top plot of Fig. 4, indicate a phase shift due to damage independent of the wind. However, the effect of damage on the blade acceleration, shown in the bottom plot of Fig. 4, is not distinguishable from the effect of wind. This is attributed to the more complex loading conditions of the blade due to the time-varying distributed load from the wind and its cyclic gravitational and wind shear load that depends on the azimuth angle of the rotor.

In the absence of an acceleration time history to distinctly reflect the effect of blade damage in spite of the wind effect, the modal properties of the blade acceleration are studied. For this, the power spectral density of the blade acceleration under steady operating conditions are studied. The motivation for this study is to capture the effect of damage on the higher frequencies independent of the wind, which is expected to affect the lower frequency acceleration (Avendano-Valencia & Fassois, 2012). For illustration purposes, the power spectral density of the first two modes of output 7 on the blade are shown for two healthy cases (Wind 1 and Wind 2) and a damaged case (Wind 1, 50% damage) in Fig. 5. The results indicate that the effect of the damage on the natural frequen-
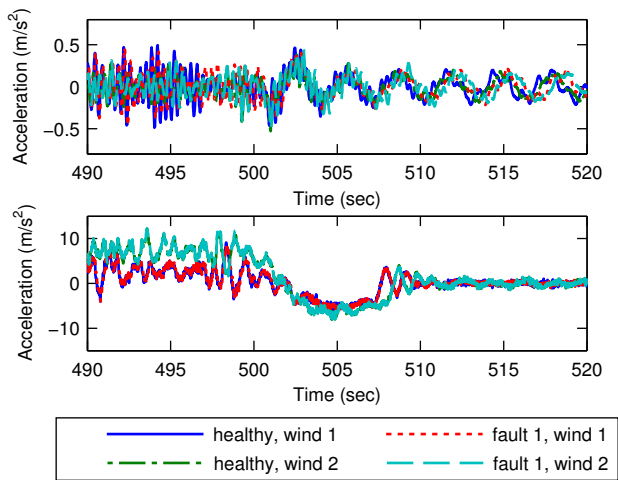
Figure 3: Acceleration of the tower at location 7 (top) and the blade at location 7 (bottom) before and after the shutdown maneuver at 500 s
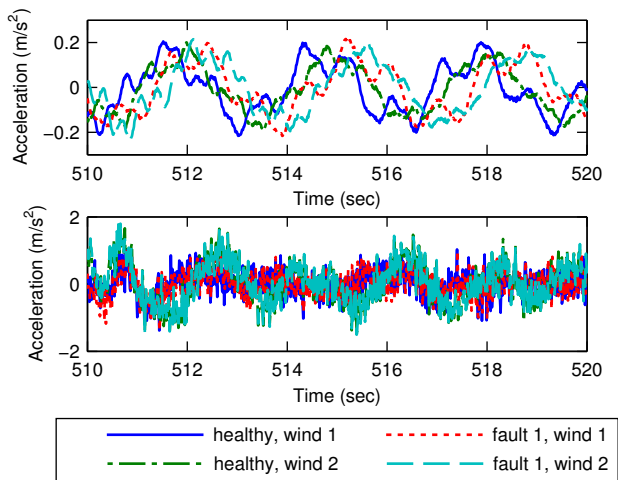
Figure 4: Acceleration of the tower at location 7 (top) and the blade at location 7 (bottom) after the brake maneuver is performed

cies of the first two modes is difficult to distinguish from the effect of wind. This motivated a study of the higher modes of acceleration in search of a more pronounced effect of the damage, independent of the wind conditions.

To evaluate the effects of wind conditions and damage on the third and fourth modes, acceleration data were generated with FAST using the third and fourth flap-wise mode shapes of the blade. The power spectral density counterparts of Fig. 5 for the third and fourth modes are shown in Fig. 6. The results in Fig. 6 indicate a more pronounced shift of the third and fourth natural frequencies caused by damage beyond any shifts by wind conditions. This observed shift in the third and fourth
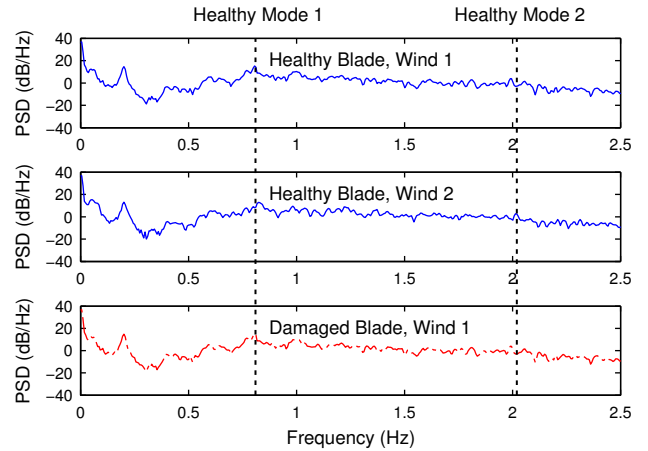
Figure 5: Power spectral density of blade acceleration at output 7. The top plot corresponds to the healthy blade excited by wind profile 1 (i.e., the baseline). The middle plot corresponds to the healthy blade excited by wind profile 2, and the bottom plot is associated with a damaged blade excited by wind profile 1. The damage consists of a 50% reduction in stiffness at the p1 nodes.

mode natural frequencies motivates the use of blade acceleration power spectral density as the dynamic response representative of blade damage. It should be noted here that tower damage could potentially be identified as well from the spectral density of its higher frequency vibration. However, such an approach is unnecessary because it is more straightforward to detect tower damage from the dynamic time response history which precludes the complexities of spectral analysis.

4. DAMAGE DETECTION METHOD

The objective of the proposed damage detection method is to provide clear and irrevocable indication of tower and blade damage of various levels by the majority of the measured accelerations with different wind speeds and profiles. To this end, it uses continuous wavelet transforms (CWTs) to represent and enhance various shape attributes of dynamic responses in order to identify the responses that are different in shape due to damage and wind. Continuous wavelet transforms have the noted feature of representing the shape attributes of transformed signals in the time-scale domain as well as the capacity to accentuate their differences (Danai et al., 2011). Therefore, they have been extensively used in structural damage detection for accentuating the effect of damage on mode shapes (Chang & Chen, 2004; Ovanesova & Suarez, 2004; Loutridis, Douka, Hadjileontiadis, & Trochidis, 2005; Rucka & Wilde, 2006). The damage detection strategy used here, instead, applies the CWTs directly to the tower dynamic time responses or blade frequency spectra to identify regions, referred to as "change signatures," in the time-scale domain or frequency-scale do-
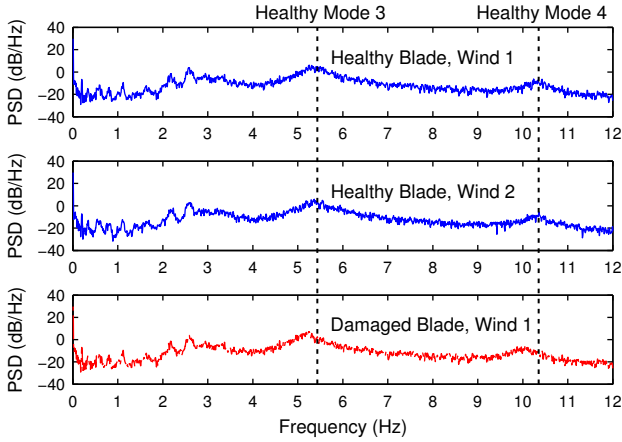
Figure 6: Power spectral density of blade acceleration at output 7 using flap-wise bending modes 3 and 4 in the FAST Model. The top plot corresponds to the healthy blade excited by wind profile 1 (i.e., the baseline). The middle plot corresponds to the healthy blade excited by wind profile 2, and the bottom plot is associated with a damaged blade excited by wind profile 1. The damage consists of a 30% reduction in stiffness at the p1 nodes.

main wherein the change in the corresponding surfaces, due to wind or damage, exceeds a dominance factor. This signal detection strategy has been shown to be effective in characterizing localized differences among the dynamic time histories of a structural model in order to establish the pattern of faults in a nine-storey building (Danai et al., 2011). In this paper, the change signatures are not independently sufficient for damage detection, since signal change may have been caused by the randomness of wind, instead. Therefore, to differentiate the effect of damage from the wind, the change signatures are evaluated further by image distances so as to identify the effect of damage by their larger image distances they produce.

4.1. Transformation to the Time-Scale Domain

Briefly, a wavelet transform (WT) is obtained by the convolution of a wavelet function $\psi_s(t)$ with the signal $f(t)$ (Mallat, 1998), as

$$W\{f\}(t,s) = f * \psi_s(t) = \int_{-\infty}^{\infty} f(\tau)\frac{1}{\sqrt{s}}\psi^*\frac{(\tau-t)}{s}\mathrm{d}\tau \quad (1)$$

where $W\{f\}$ denotes the WT of the time function f, $*$ denotes convolution, ψ^* is the complex conjugate of ψ, $\psi_s(t) = \frac{1}{\sqrt{s}}\psi(\frac{t}{s})$ represents the wavelet function, and t and s denote the time (translation) and scale (dilation or constriction) parameters, respectively. The wavelet function can be manipulated in two ways: (i) it can be moved sideways (translated) to coincide with different segments of the signal, and (ii) it can be widened (dilated) or narrowed (constricted) to align with a larger or smaller segment of the signal at its current location (current time). The wavelet coefficients $W\{f\}$

that result from the convolution integral of Eq. (1) at each time (t) and scale (s) denote the cross-correlation between the wavelet function $\psi_s(t)$ and time function $f(t)$, with the wavelet function positioned at time t and dilated at scale s. Numerically, the computation of WTs is facilitated for dyadic time data. Here, we have chosen to use 128 data points; i.e., $t_k = t_1 \ldots t_{128}$ of each dynamic response to obtain the WTs for 72 scales; i.e., $s_l = s_1 \ldots s_{72}$. These choices result in a time-scale plane of 128×72 pixels, each pixel (t_k, s_l) having unity time and scale dimensions. For illustration purposes, the wavelet transform of the tower acceleration time signal at location 7 is shown in Fig. 7.
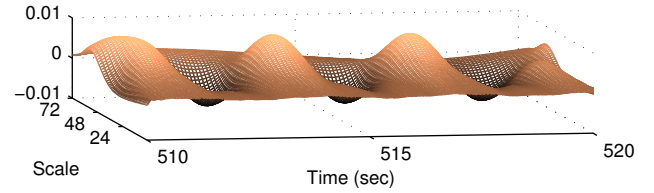
Figure 7: Gauss WT of tower acceleration at location 7 after the shutdown maneuver is performed

4.2. Representation of Shape Attributes

Representation of shape attributes of time signals by CWTs stems from their multiscale differential feature (Mallat, 1998). Consider $\psi(t)$ to be the nth order derivative of the smoothing function $\beta(t)$; i.e.,

$$\psi(t) = (-1)^n \frac{d^n(\beta(t))}{dt^n} \quad (2)$$

then this wavelet transform is a multiscale differential operator of the smoothed function $f * \beta_s(t)$ in the time-scale domain (Mallat & Hwang, 1992); i.e.,

$$W\{f\}(t,s) = s^n \frac{d^n}{dt^n}(f * \beta_s(t)) \quad (3)$$

Using this feature, one can utilize the CWT to represent the first derivative of a time signal for its slope, or its second derivative to represent the rate of slope change. For instance, one may consider the smoothing function $\beta(t)$ to be the Gaussian function. In this case, the Gauss wavelet is the first derivative of the Gaussian function. This results in a wavelet transform that is the first derivative of the signal $f(t)$ smoothed by the Gaussian function, and orthogonal to this smoothed signal. Similarly, the Sombrero wavelet is the second derivative of the Gaussian function, and produces a wavelet transform that is the second derivative of this smoothed signal in the time-scale domain. Therefore, the Gauss WT represents the Gaussian smoothed slope of the signal $f(t)$ and the Sombrero WT denotes its rate of slope change.

4.3. Delineation of Localized Dissimilarities

For a view of the delineation capacity of CWTs, which is of significance to this research, let us consider the WT of a time signal $f(t)$ at a particular coordinate (t_1, s_1):

$$W\{f\}(t_1, s_1) = \int_{-\infty}^{\infty} f(\tau) \frac{1}{s_1} \psi \left(\frac{t_1 - \tau}{s_1} \right) d\tau \quad (4)$$

The wavelet coefficient, $W\{f\}(t_1, s_1)$, which represents the cross-correlation of $f(t)$ with $\psi_{s_1}(t_1)$, depends upon the magnitude of $f(t)$ as well as the conformity of $f(t)$ with the shape of the dilated $\psi_{s_1}(t_1)$. Therefore, the wavelet coefficients can accentuate minute differences between time signals at the lower scales by capturing the conformity of a narrow $\psi_s(t)$ with a small segment of the time signal.

To illustrate the enhanced delineation provided by CWTs, let us consider the highly correlated pairs of acceleration signals ($\rho = 0.9830$) shown in the top plot of Fig. 8. The two signals are different due to a damage. Although the two signals have near identical shapes, as represented by their correlation coefficient, they have distinct local differences that can be accentuated by their wavelet coefficients. The points of deviation between the slopes of the two signals are accentuated by the differential Gauss wavelet coefficients in the bottom plot of Fig. 8. The peaks and valleys in the plot are reflections of the differences in the slopes of the two signals in the top plot of the figure. Whereas such local dissimilarities are masked by a lumped measure such as the correlation coefficient, the pixels associated with these peaks and valleys mark the regions of slope difference between the two signals. Therefore, the analysis can be focused on where the difference is prominent. As a result of the enhanced delineation described above, regions of significant deviation between two signals; i.e., the signal and its baseline, can be identified to characterize the effect of wind or damage on the signal.

4.4. Signature Extraction

For signal change detection, the change (due to wind or damage) in a dynamic response (tower acceleration history or blade power spectral density) is identified by comparing the wavelet coefficients of the response with those of their baseline. Change identification is performed by isolating regions of the corresponding plane (comprised of the sample points $t_k, k = 1, \ldots, N$ and scales: $s_l, l = 1, \ldots, M$) wherein a dynamic response deviates from the undamaged response by a *dominance factor*, η_d. The union of the isolated regions associated with a dynamic response is called the 'change signature,' formally defined for the jth sensor location as the union of all pixels $(t_k^j, s_l^j) \in \delta_j$ in the plane wherein the nonzero (relative to the threshold h) normalized wavelet coefficient of the output y_j exceeds the normalized wavelet coefficient of its baseline y_j^n by a dominance factor η_d, expressed mathe-
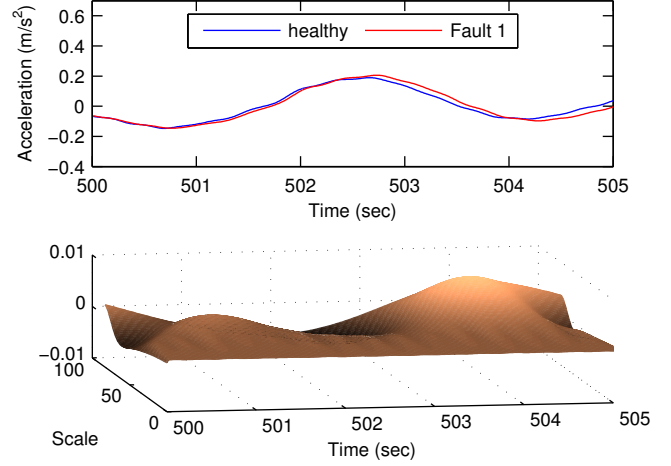
Figure 8: Illustration of the enhanced delineation of two similar signals (top) by the differential wavelet transform (bottom) which accentuates the minute differences between the two signals

matically as

$$\left| \overline{W\{y_j\}}(t_k, s_l) \right| > h > \eta_d \left| \overline{W\{y_j^n\}}(t_k, s_l) \right| \implies$$
$$(t_k, s_l) = (t_k^j, s_l^j) \in \delta_j \quad (5)$$

where

$$\overline{W\{y_j\}} = \frac{W\{y_j\}}{\max_{(t,s)} |W\{y_j\}|} \quad (6)$$

If the above condition is satisfied at a pixel (t_k, s_l), then we tag the pixel as (t_k^j, s_l^j) to note its inclusion in the change signature δ_j. The inclusion of the threshold, h, in Eq. (5) is a provision to exclude pixels at zero crossings of the dynamic response wavelet coefficients. Without this provision, at zero-crossings (e.g., when the Gauss wavelet coefficients are zero due to zero slopes at the peaks of the acceleration signals) any nonzero wavelet coefficient would dominate this zero wavelet coefficient and hence include superfluous pixels in the corresponding damage signature. We have found the value of $h = 0.005$ to be sufficient as a safeguard against inclusion of zero-crossing pixels in the change signatures. The other factor in the change signature extraction routine of Eq. (5) is the dominance factor, η_d. Since higher dominance factors lead to fewer pixels in the change signature at the risk of missing minute differences between the dynamic responses, higher dominance factors correspond to higher standards of change detection.

For illustration purposes, change signatures between the two healthy signals (healthy, wind 1 and healthy, wind2) in Fig. 4 are shown in the top plot of Fig. 9. For comparison, also shown in Fig. 9 (bottom plot) are the change signatures of the faulty signal (fault 1, wind 1 and healthy, wind 1) in Fig. 4.

Shown in this figure, are two sets of signatures, marked as blue and red. The blue signatures are associated with

$$\left|\overline{W\{y_j^n\}}(t_k, s_l)\right| > h > \eta_d \left|\overline{W\{y_j\}}(t_k, s_l)\right| \implies (t_k, s_l) \in \delta_j^n$$

and the red signatures correspond to

$$\left|\overline{W\{y_j\}}(t_k, s_l)\right| > h > \eta_d \left|\overline{W\{y_j^n\}}(t_k, s_l)\right| \implies (t_k, s_l) \in \delta_j$$

The change signatures in Fig. 4 are clearly farther apart for the faulty signal than those for the healthy signal, represented by the larger lag caused by the damage in contrast to the wind.
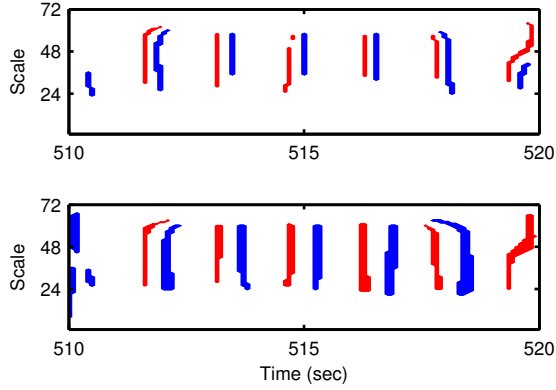
Figure 9: Change signatures between two signals from a healthy tower with different wind conditions (top) and those between a signal from a faulty tower and a healthy signal (bottom)

4.5. Image Distances of Damage Signatures

Since the change signatures only characterize the change of the signal, they are bound to be generated under normal conditions because of the wind. Accordingly, a separate measure is required to differentiate between the change signatures caused by wind and those by damage. As was shown visually in Figs. 4 and 6, the differentiating aspect of the two effects is the larger lag that is caused by the damage in contrast to the wind. To characterize this aspect, image distances are utilized to represent the distance of the change signatures.

To assess the distances between the change signatures, either the Euclidean distance or the weighted Euclidean distance (also known as image Euclidean distance (Wang, Zhang, & Feng, 2005)) can be used. However, our analysis indicates that the weighted Euclidean distance provides a more succinct distance measure because of its assignment of larger weights to pixels of higher proximity to each other. The weighted Euclidean distance, d_I, hereafter referred to as imaged distance, discounts the difference in magnitudes of wavelet coefficients according to the mutual distance between their locations on the time-scale plane, as (Wang et al., 2005)

$$d_I^2(\delta_j, \delta_j^n) = \frac{1}{2\pi\sigma^2} \sum_{k=1, l=1}^{N,M} \exp\{-|P_k - P_l|^2/2\sigma^2\}$$

$$(W\{\delta_j\}_k - W\{\delta_j^n\}_k)(W\{\delta_j\}_l - W\{\delta_j^n\}_l) \qquad (7)$$

where σ is a width parameter that represents the discount rate associated with the pixel distance, k and l denote the coordinates of each pixel on the time-scale or frequency-scale plane, P_k and P_l denote pixel locations, and $|P_k - P_l|$ represents the distance between two pixels on the plane lattice. According to Eq. (7), the image distance fully incorporates the difference in magnitude of wavelet coefficients with identical locations and discounts by the weight "$\exp\{-|P_k - P_l|^2/2\sigma^2\}$" the magnitude difference when the two locations do not coincide on the time-scale or frequency-scale plane (i.e., image lattice).

For the application of image distances to damage detection, consider the Gauss WT of the tower acceleration shown in Fig. 7 in the time-window of 510-520 s after the shutdown maneuver (at 500-508 s). The surface consists of a series of peaks and valleys at higher scales. This results in a recurring set of vertical signatures shown in Fig. 9. Given that these signatures may have been caused by wind or damage, the distinction between them is clarified through the distances between the signatures. However, change signatures could also be caused by noise or the edge effects of wavelet transform. Therefore, image distances should be ideally computed for the change signatures that are representative of wind or damage. Referring to Fig. 9, an image distance computed for a single pair of change signatures would be sufficient for representing the cause of change. To facilitate this focus on the signature pairs, a window in the corresponding plane is considered, as shown in Fig. 10, to isolate a few pairs of change signatures for computation of the image distance.
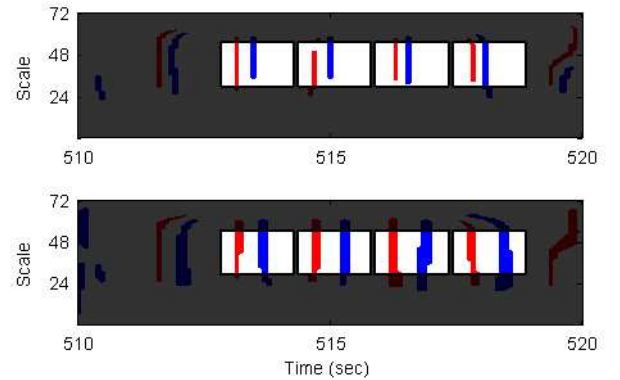
Figure 10: The change signatures in Fig. 9 enclosed by a window in the time-scale domain to better capture the area of relevance to the change

5. DAMAGE ESTIMATES

The possibility of estimating tower and/or blade damage by image distances was studied by transforming the acceleration records (the tower acceleration time histories or the blade ac-

celeration power spectral densities) via the Gauss or Sombrero WT into their corresponding domains and then extracting their change signatures using the acceleration from the healthy turbine with the wind 1 profile as the baseline. This was also performed for the acceleration records obtained with the other wind profiles. The success of damage estimation by this method was then verified by obtaining larger image distances for the acceleration signals from the damaged turbine in comparison to those from the healthy turbine under different wind conditions. The analysis was performed using Gauss WT, for tower damage detection, and Sombrero WT, for blade damage detection. However, the analysis is not specific to the WT, as either WT could be used for detection of tower or blade damage.

5.1. Tower Damage Estimates

Image distances were obtained for the tower acceleration time histories obtained at different locations. The acceleration records of the healthy and damaged tower obtained with different wind profiles were transformed to the time-scale domain by the Gauss WT. Change signatures were then extracted at the dominance factor of $\eta_d = 6$ for the acceleration signals of the healthy and damaged tower in the time window of 510 to 520 seconds, using the acceleration of the healthy tower with wind 1 as the baseline.

For successful damage estimation, the images distances from the damaged tower need to be higher than those from the healthy tower, albeit with different wind profiles. To test this hypothesis, the image distances of the acceleration signals from the healthy tower (different winds) at its nine output locations are compared with those from the 5% damaged tower in Fig. 11. In all these cases, the wind profiles had a mean speed of 12 m/s. The image distances in Fig. 11 are clearly larger for the damaged tower than the healthy tower. This validates the premise of the method that image distances can discern the effect of damage from the wind on acceleration time histories of the tower.

The next issue to be addressed is the effect of damage level on the image distances. To address this point, the image distances obtained with different damage levels from the acceleration at output location 7 of the tower are shown in Fig.12 with different wind profiles. The results indicate that the image distances provide consistent and reliable estimates of the damage regardless of the damage level across different wind profiles. However, the magnitudes of damage distances do not seem to be affected by the damage level.

Yet another issue to be explored is the influence of the mean wind speed on damage estimation. Since wind is the single most important factor in acceleration of the wind turbine, it is likely to provide higher excitation levels at higher speeds. On the other hand, at higher than the rated wind speed, the control system will pitch the blade so as to maintain constant power. Accordingly, three wind speeds of 6, 12, and 18 m/s were se-
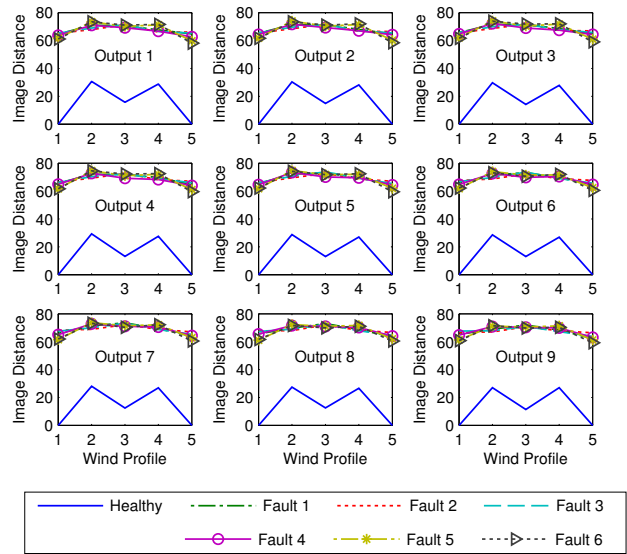
Figure 11: Image distances of the acceleration time histories at 9 output locations of the tower obtained for the healthy tower and a 5% damaged tower with five different wind profiles having a mean speed of 12 m/s
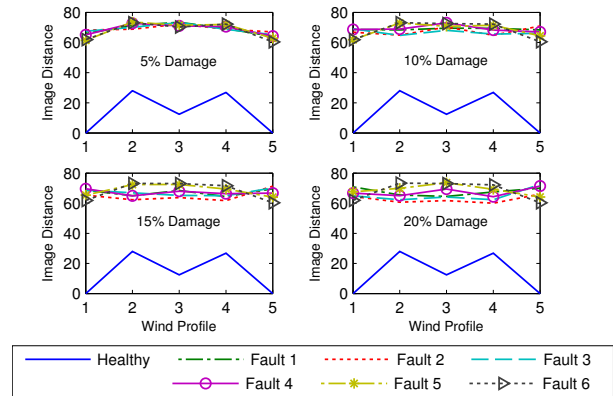
Figure 12: Image distances with varying levels of damage obtained from the acceleration time histories at output location 7 of the tower with different wind profiles having a mean speed of 12 m/s

lected within the operating range of the wind turbine. The image distances obtained with different wind speeds from the acceleration at output location 7 of the tower for both the 5% damaged and healthy tower are shown in Fig. 13 for different wind profiles. The image distances indicate that damage can still be reliably estimated at these other wind speeds, albeit at a lower margin than those achieved at 12 m/s. At the mean wind speed of 6 m/s, the image distance of the damaged tower is quite close to that of the healthy tower with wind profile 3. Similarly, at the mean wind speed of 18 m/s, the image dis-

tance of the healthy tower with wind profile 5 is within the range of those considered to be representative of the damage.
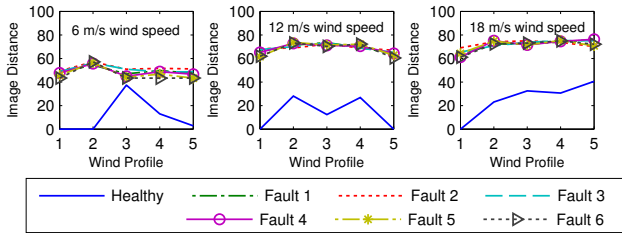
Figure 13: Image distances at different mean wind speeds obtained from the acceleration time histories at output location 7 of the tower for the healthy and 5% damaged tower with different wind profiles

5.2. Blade Damage Estimates

The acceleration used for blade damage estimation was obtained during normal operation, since the dynamic response of interest was the power spectral density of the third and fourth mode acceleration. Therefore, there was no shutdown maneuver necessary as a standardized excitation. Blade damage was estimated from the power spectral density of the blade acceleration at different blade locations. For blade acceleration, the Sombrero WT was used to provide peaks and valleys similar in location to those of the actual acceleration. Also, instead of the acceleration time history that was used for the tower, the windowed spectra of the blade acceleration were used for representation of acceleration in the frequency-scale domain. For illustration purposes, the wavelet transform of the spectrum of blade acceleration at output location 7 of the blade for the healthy blade, excited by wind profile 1, is shown in Fig. 14. The surface of the WT is shown in the top plot of Fig. 14 and its contour in the bottom plot. The wavelet transform is created using the Sombrero wavelet and results in ridges around the third and fourth flap-wise natural frequencies.

The effect of damage and wind on the Sombrero WT of the frequency spectra is shown in Fig. 15 for the blade acceleration at output location 7. The top plot corresponds to the healthy blade excited by wind profile 1 (i.e., the baseline). The middle plot corresponds to the healthy blade excited by wind profile 2, and the bottom plot is associated with a 30% damaged blade excited by wind profile 1. The baseline (top) plot is very similar to the middle plot which is associated with the healthy blade as well. But the bottom plot contains a significant off-set (shift) relative to the other two as the result of the damage. It should be noted that this off-set is also observed in the frequency spectra of Fig. 6, which are the sources of the contours in Fig. 15. Therefore, one may be tempted to perform damage estimation from the offset between the frequency spectra peaks. However, as is shown
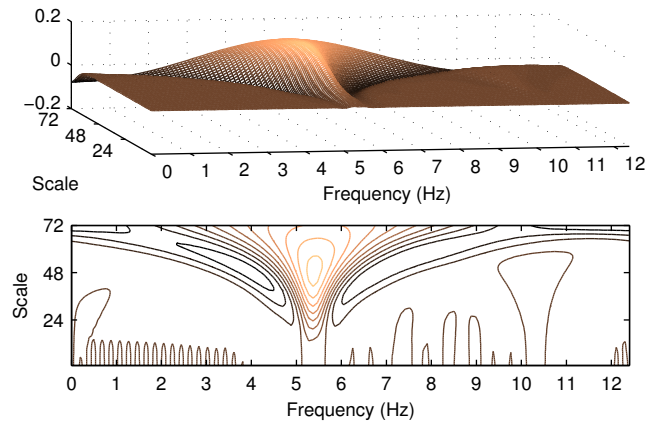
Figure 14: Sombrero WT of the healthy blade acceleration at output location 7 of the blade excited with wind profile 1 (top) and its contour in the frequency-scale plane (bottom)

later in the Discussion section, such an estimation technique does not provide nearly as robust a set of results as those by the image distances of the change signatures. The advantage of relying on the WT of the frequency spectra stems from the multi-resolution image of the signal provided at various scales, which enhances identification of the natural frequency over peak picking in the frequency domain.
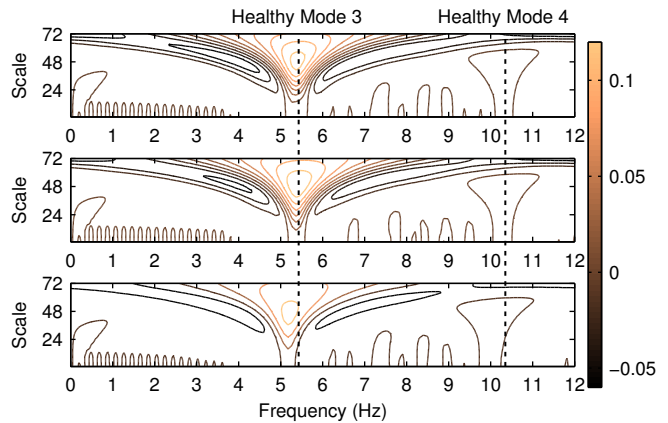
Figure 15: Contour plots of the sombrero WT of the blade acceleration at output location 7 of the blade. The top plot corresponds to the healthy blade excited by wind profile 1 (i.e., the baseline). The middle plot corresponds to the healthy blade excited by wind profile 2, and the bottom plot is associated with a 30% damaged blade excited by wind profile 1.

Change signatures were obtained from the Sombrero WTs of the blade acceleration power spectra, but at a lower dominance factor of $\eta_d = 1.4$. The change signatures obtained from the healthy (wind 2) and damaged (wind 1) blade accelerations at output location 7 of the blade, depicted in the middle and bottom plots of Figs. 6 and 15, with the acceleration

of the healthy blade (wind 1) as baseline (i.e., corresponding to top plot of these figures) are shown in Fig. 16. It is clear from the results that the damaged blade produces far more change signatures.
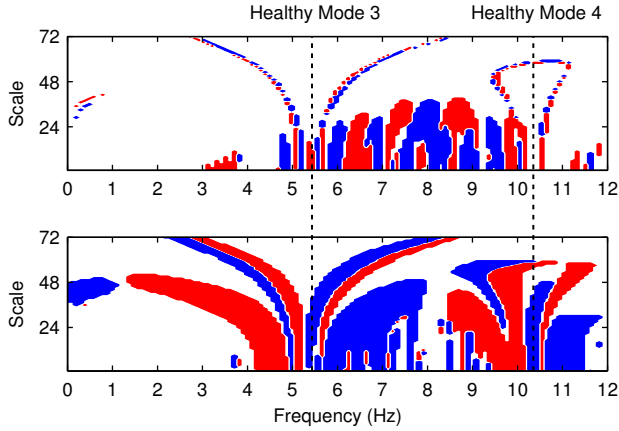
Figure 16: Change signatures of the Sombrero WT of the acceleration at blade output location7. The top plot represents the difference between the healthy blade acceleration excited by wind profile 2 relative to the acceleration by wind profile 1, used as baseline. he bottom plot represents the difference caused by 30% damage with the same wind excitation as the baseline.

To compute the image distances for the blade acceleration, a larger window than the window used for the tower acceleration was required, to encompass modes 3 and 4. Furthermore, the computation window was positioned at higher scales than the one for the tower to mitigate the effect of noise at lower scales. For illustration purposes, the windows used for computing the image distances of the blade acceleration at each of the modes 3 and 4 are shown in Fig. 17.

The image distances of the change signatures obtained separately for the third and fourth modes from each output location of the blade are shown in Figs. 18 and 19, respectively. Unlike the results for the tower, which were consistent across all output locations, the image distances for the blade are not the same for all output locations. For instance, output location 1 at the root of the blade does not seem to provide the distinction between the damaged and healthy blades that output location 7 provides, for example. Nevertheless, in most cases the damage seems to be decipherable with adequate margins between the image distances of the damaged and healthy blade.

As with the tower, image distances were obtained for different levels of blade damage, to evaluate the capacity of the image distances in characterizing the level of damage. The image distances obtained from modes 3 and 4 of output location 7 acceleration for different damage levels are shown in Fig. 20. The image distances not only provide adequate margins for
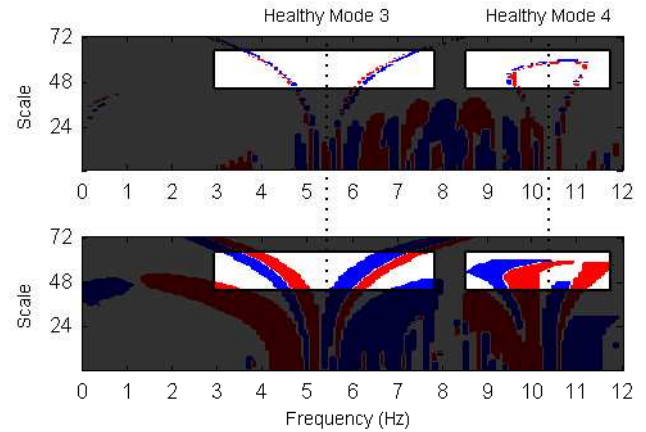
Figure 17: Windows (white areas) defined in the frequency-scale plane to focus image distance computation of the change signatures for blade acceleration around the third and fourth mode natural frequencies
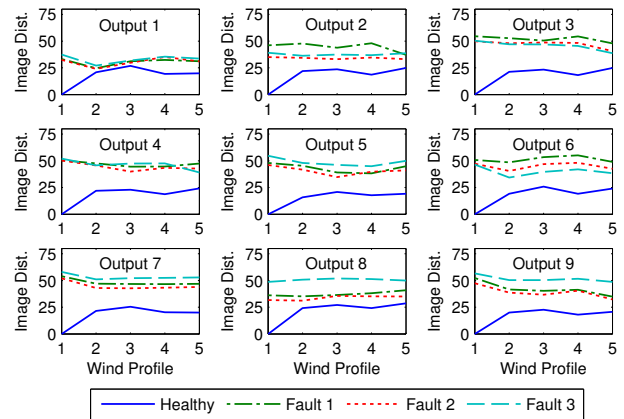
Figure 18: Image distances of the change signatures in the proximity of the third mode for the healthy and 30% damaged blade by each of the nine blade output locations

damage estimation beyond 10% damage (10% reduction in stiffness coefficient), but also indicate the level of damage. This is in contrast to the image distances from the tower in Fig. 12, which were insensitive to the damage level.

To evaluate the influence of wind speed on the damage estimation results, image distances were also obtained for the change signatures of modes 3 and 4 accelerations of blade output location 7 with two other mean wind speeds at 6m/s and 18 m/s. The image distances from the three mean wind speeds are shown in Fig. 21. The results indicate that mode 3 provides a more consistent basis for damage estimation across different wind speeds and that the largest margin exists at the lowest wind speed of 6 m/s. This could be due to the absence of pitch control at this lower speed and lower turbulence.
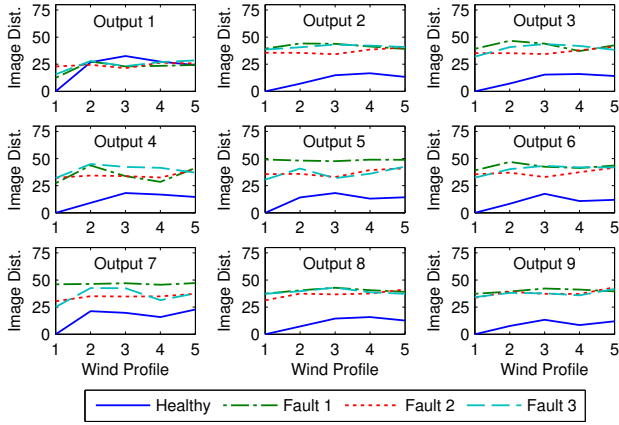
Figure 19: Image distances of the change signatures in the proximity of the fourth mode for the healthy and 30% damaged blade by each of the nine blade output locations

6. DISCUSSION

The results presented above indicate the effectiveness of the method in estimating the tower and blade damage in presence of varying wind conditions. The method relies on several factors which enhance its robustness, including its use of wavelet transforms to accentuate the delineation of vibration signals, its change signature mechanism that allows selective detection of effect levels, and the capacity to use windows for exclusion of noise effects. Nevertheless, the question remains as whether similar performance can be obtained by a far simpler method such as peak picking in either time or frequency domains. To address this point, we performed blade damage estimation by peak picking in the frequency domain using the frequency spectrum of blade acceleration containing the third and fourth modes. For this, the frequency spectra were low-pass filtered to smooth their edges and the third or fourth mode frequency was estimated by finding the local maximum of the spectrum within the frequency window associated with the mode. The distance of the estimated frequency from its baseline was then used as the damage estimate, as shown in Fig. 22. The results indicate that although the frequency distances at locations 1, 2 and 7 provide adequate differentiation between the damage and wind effects, the distances at the other locations are not as distinct. These distances were also found to be sensitive to the level of smoothing and generally less robust to fault locations and different wind speeds. The multi-scale smoothing of the signal provided by the wavelet transforms is considered to be an important factor, among others, in the added robustness of the proposed method.

The results from the proposed method also indicate that while the image distances are sensitive to the level of damage, the location of blade damage, and the operating conditions (wind speed and profile), they provide overall margins that effectively distinguish the effect of damage from the wind. The results further indicate that unlike the tower damage estimates,
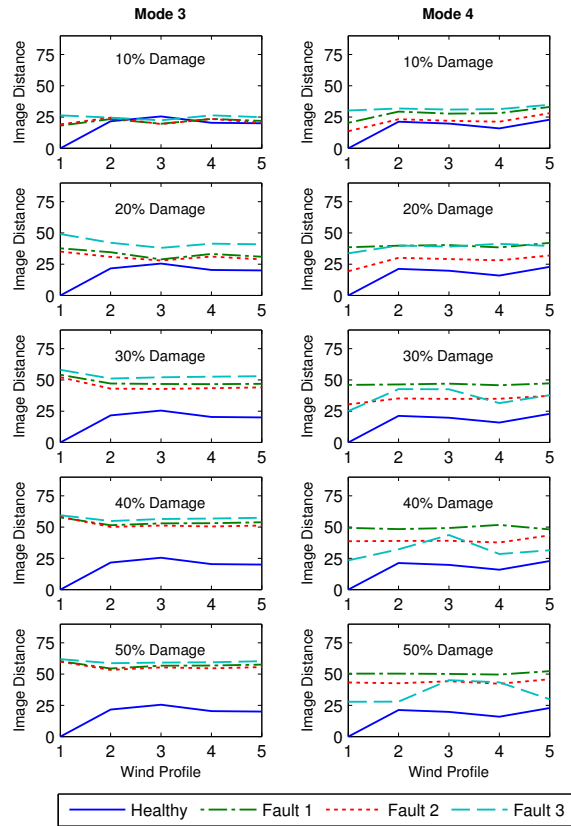
Figure 20: Image distances of the change signatures from the third and fourth modes of the healthy and different level damaged blades using the acceleration of blade output location 7 with wind profiles having the mean wind speed of 12 m/s

the blade damage estimates are sensitive to sensory location. This is due to the fact that the motion of the tower is dominated by the first mode acceleration and therefore all of the sensory locations produce similar results. The acceleration of the blade, on the other hand, is studied in proximity of the third and fourth modes. As a result, the sensors that are close to the nodes of either mode do not provide reliable information. For instance, the blade damage estimates in Figs. 18 and 19 from output location 1 of the blade, close to its root, are generally inferior to the others. This is due to the absence of acceleration at this point and the FAST model, which represents the connection between the blade and the hub as rigid. As to the algorithmic issues not studied in this paper and the concerns associated with the practical application of the method, the following points warrant further investigation.

- *Algorithmic Issues:*
  - Width parameter: Adjustment of the image distance width parameter, σ, in Eq. (7) affects how pixels are discounted due to distance. For the tower and the blade, a $\sigma = 1$ was used. However, the change
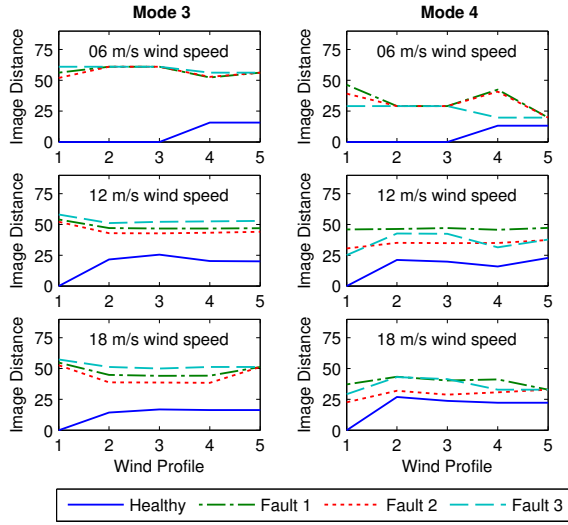
Figure 21: Image distances of the change signatures according to the third and fourth modes computed from the acceleration of blade output location 7 for the healthy and 30% damaged blade at different mean wind speeds
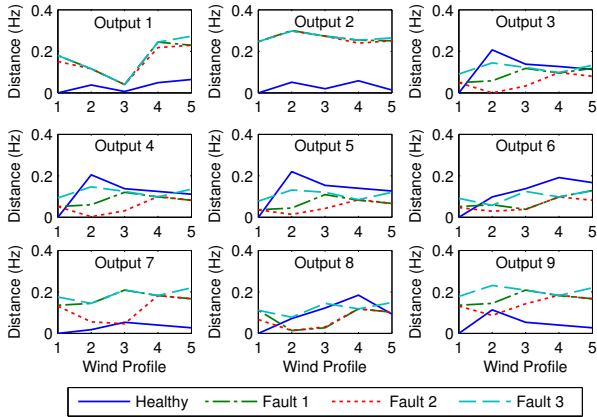
Figure 22: Frequency distances caused by different 12 m/s mean wind speed profiles and 30% blade damage according to peak picking of the power spectral density of blade acceleration at the nine output locations of the blade

signatures are further apart for the tower than the blade. Therefore, fine tuning of the width parameter might lead to improved results.

– Dominance factor: A range of dominance factors, η_d in Eq. (5), were tested for each damage estimation case. A higher dominance factor generally resulted in change signatures with fewer pixels and the corresponding image distances which were less sensitive to the wind profile.

– Windowing: Windows are used to focus image distance estimation on the areas of plane where change

signatures are representative of mostly damage. In the case of the tower, the change signatures represent the cyclic nature of the response, therefore, the windows are placed to capture signature pairs. Accordingly, the location of the windows depend on the wavelet transform used for damage estimation. For the case of the blade, on the other hand, the windows need to be positioned around the third and fourth mode natural frequencies. Therefore, apart from slight adjustments for the dominance factor used, the window needs to be placed in the middle of the scale range to avoid noise, which is mostly present at low scales (high frequency), and edge effects, which usually appear at higher scales (low frequency).

• *Application Concerns:*

– Measurement noise: In practice, measurement noise will influence the dynamic response. However, we do not expect it to significantly affect the performance of the method, because of the several provisions of the method that enable it to cope with the stochastic nature of dynamic responses. One such provision is the capacity to exclude low-scale (high-frequency) regions of the plane from the image distance window, so as to minimize the influence of noise. Another provision is the dominance factor, η_d in Eq. (5), which allows exclusion of small changes caused by noise from the change signatures. In general, the varying wind conditions with which this method is designed to cope are considered to be much more problematic than measurement noise, because of their low frequency nature that coincides with the acceleration signals of interest in the 0.3 - 12 Hz range.

– Modal analysis of the blade vibration: These simulations have been performed using the third and fourth flap-wise blade natural frequencies. FAST is only able to model two flap-wise and one edge-wise mode of vibration per simulation. In contrast, the real system will contain all modes of vibration in its dynamic response, wherein the lower modes dominate. Therefore, it may be more difficult to extract the third and fourth mode properties, hence the shifts of the third and fourth mode frequencies. To provide a preliminary evaluation of the potential challenge posed by such condition, simulation runs were conducted in FAST using the first and third modes together in one case, and the first and fourth modes together in another case. The frequency spectrum of each of these simulation runs is compared in Fig. 23 to the frequency spectrum of the dynamic response obtained using the third and fourth modes. The results in this figure do

not show a significant diminishment of the third or fourth modal estimation due to the presence of the 1st mode in the dynamic response. Another issue not considered in the present study, due to the limitation of FAST, is modal coupling due to the twist of the blades.
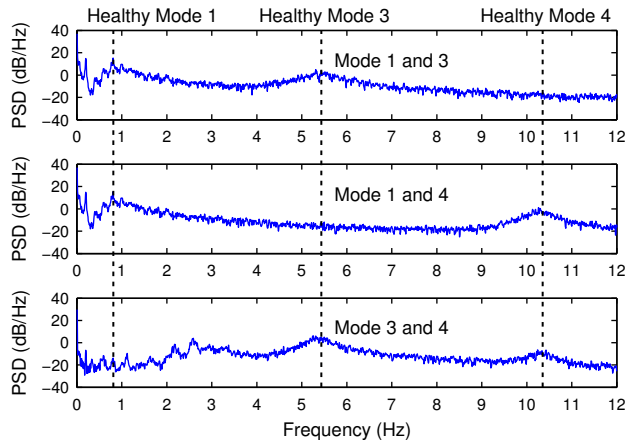
Figure 23: Comparison of the blade spectra of three different scenarios each containing only two of the flap-wise mode shapes: modes 1 and 3 in the top plot, modes 1 and 4 in the middle plot, and modes 3 and 4 in the bottom

– Sensor location: The insensitivity of tower damage estimates to sensor location suggests that a single sensor may be sufficient for tower damage detection. The blade damage estimates, however, are more nuanced. Certain sensors perform better at detecting damage using the third mode of vibration. Others perform better using the fourth mode of vibration. This warrants further analysis to ascertain the optimal location of sensors and their numbers for robust and reliable damage estimation.

– Type of sensor: Although the data used in this research is based on simulated accelerometer data, the results are not expected to be constrained by the type of data. Strain gauge data is likely to be as suitable for the analysis.

– Data acquisition constraints: Since identification of tower damage in this paper is based on the tower dynamic response time history, there will be no sampling constraints on the data acquisition system so long as the time histories capture the phase shift caused by damage. However, identification of blade damage is based on at least the third mode of vibration, so the sampling frequency needs to be high enough to capture this mode. Given that the storage requirements for such high frequency data may prove to be infeasible, one could consider analyzing

the data right after data acquisition and discarding it once the system is evaluated as healthy.

– Wind profiles: This study has examined three wind speeds. At each wind speed, five full field, turbulent wind profiles were used to test the effect of wind on the dynamic response. However, this topic should be studied further to determine if the method can handle wind files which are even more dissimilar. It is also desirable to perform a full scale validation of the method.

– Model Accuracy: The results presented in this paper have been obtained with utmost attention to the intricacies of the problem. To this end, the model of the wind turbine has been configured to account for power regulation by the pitch controller and the aerodynamics of the blades as well as the 3D dynamics of the blades, the tower, the drive train, the generator, the yaw system. Beyond these results, a more realistic validation of the methods needs to rely on experimental data.

7. CONCLUSION

A unified method of damage estimation is introduced for blade and tower damage detection of operating wind turbines. For tower damage estimation, the acceleration time response of the tower to a shutdown maneuver is considered, and for blade damage estimation, the blade frequency spectrum of the third and fourth modes of acceleration. For damage estimation, pairwise change signatures are extracted from the continuous wavelet transforms of the dynamic responses and their image distances are used for damage estimation. The performance of the method is studied based on simulated acceleration of the NREL 5 MW wind turbine using the aero-elastic design code FAST. The results indicate that the method provides robust damage estimates in presence of varying wind with the acceleration records of various sensory locations of the tower and blade. Furthermore, the tower damage estimates are shown to be insensitive to the damage level, whereas the blade damage estimates represent the damage level as well.

REFERENCES

Avendano-Valencia, L., & Fassois, S. (2012). In-Operation Output-Only Identification of Wind Turbine Structural Dynamics: Comparison of Stationary and Non–

Stationary Approaches. In *ISMA Conference on Noise and Vibration Engineering.* Leuven, Belgium.

Buhl, M. (n.d.). *NWTC Design Codes.* `http://wind.nrel.gov/designcodes/preprocessors/modes/.` (Last modified 26-May-2005; accessed 24-January-2012)

Carden, E., & Fanning, P. (2004). Vibration based condition monitoring: a review. *Structural Health Monitoring*, *3*(4), 355–377.

Chang, C., & Chen, L. (2004). Damage detection for a rectangular plate by spatial wavelet based approach. *Applied Acoustics*, *65*, 819-832.

Danai, K., Civjan, S. A., & Styckiewicz, M. M. (2011). Direct method of damage localization for civil structures via shape comparison of dynamic response measurements. *Computers & Structures*.

Danai, K., & McCusker, J. R. (2009). Parameter estimation by parameter signature isolation in the time-scale domain. *ASME J. of Dynamic Systems, Measurement and Control*, *131*(4), 041008.

Doebling, S. W., Farrar, C. R., Prime, M. B., & Shevitz, D. W. (1996). *Damage identification and health monitoring of structural and mechanical systems from changes in their vibration characteristics: a literature review* (Tech. Rep.). Los Alamos National Lab., NM (United States).

Farrar, C. R., & Doebling, S. W. (1997). An overview of modal-based damage identification methods. In *Proceedings of DAMAS Conference* (pp. 269–278).

Friswell, M. I. (2007). Damage identification using inverse methods. *Philosophical Transactions of the Royal Society A: Mathematical, Physical and Engineering Sciences*, *365*(1851), 393–410.

Jonkman, J., & Buhl Jr, M. (2005). FAST users guide. *Rep. No. NREL/EL-500-38230, NREL, Golden, Colorado, USA*.

Jonkman, J., Butterfield, S., Musial, W., & Scott, G. (2009). Definition of a 5-MW reference wind turbine for offshore system development. *National Renewable Energy Laboratory, NREL/TP-500-38060*.

Kelly, N., & Jonkman, B. (n.d.). *NWTC Design Codes.* `http://wind.nrel.gov/designcodes/preprocessors/turbsim/.` (Last modified 03-February-2011; accessed 17-July-2012)

Loutridis, S., Douka, E., Hadjileontiadis, L., & Trochidis, A. (2005). A two-dimensional wavelet transform for detection of cracks in plates. *Engineering Structures*, *27*, 1327–1338.

Mallat, S. (1998). *A wavelet tour of signal processing. 1998.* Academic, San Diego, CA.

Mallat, S., & Hwang, W. L. (1992). Singularity detection and processing with wavelets. *Information Theory, IEEE Transactions on*, *38*(2), 617–643.

Ovanesova, A., & Suarez, L. (2004). Applications of wavelet transforms to damage detection in frame structures. *Engineering Structures*, *26*, 3949.

Rucka, M., & Wilde, K. (2006). Application of continuous wavelet transform in vibration based damage detection method for beams and plates. *Journal of Sound and Vibration*, *297*, 536–550.

Santos, J. A. dos, Maia, N., Soares, C. M., & Soares, C. M. (2008). Structural damage identification: a survey. *Trends in computational structures technology, Saxe-Coburg Publications, Stirlingshire, UK*, 1–24.

Wang, L., Zhang, Y., & Feng, J. (2005). On the Euclidean distance of images. *Pattern Analysis and Machine Intelligence, IEEE Transactions on*, *27*(8), 1334–1339.